



# Low Temperature Plasma Technology Laboratory

---

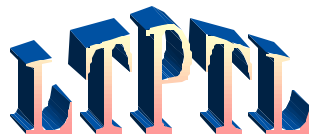
## **CHARACTERIZATION AND MODELING OF THE MØRI SOURCE**

Francis F. Chen and Donald Arnush

FINAL REPORT, UC MICRO PROJECT 98-020  
JOINTLY FUNDED BY APPLIED MATERIALS

LTP-002

February, 2000



Electrical Engineering Department  
Los Angeles, California 90095-1594

# CHARACTERIZATION AND MODELING OF THE MØRI SOURCE

Francis F. Chen and Donald Arnush

Electrical Engineering Department  
University of California, Los Angeles, California, 90095-1594

Final Report 1998-99 for MICRO Project 98-020  
Industrial Sponsor: Applied Materials, Inc.

## ABSTRACT

A user-friendly computer code, HELIC, was developed to model helicon discharges; it was used to predict the behavior of the MØRI source as various parameters are changed. With another code, it is shown how the magnetic field pattern can be changed to optimize operation. In addition, theoretical insights were gained on the injection of plasma from a helicon source into a working chamber, and on the transition between ICP (Inductively Coupled Plasma) and HWS (Helicon Wave Source) operation.

## INTRODUCTION

The MØRI<sup>®</sup> source (M = 0 Reactive Ion etcher) is a commercial helicon plasma source developed at PMT, Inc. (now Trikon) and licensed to Applied Materials and Lam Research. Its properties have been documented in two recent papers [1, 2]. Etch tools based on this source achieved excellent results in industrial laboratories before the PMT facility was closed. The superiority of HWS over ICP tools stems from two main features: (a) the shape of the DC magnetic field  $\mathbf{B}_0$  can be changed to maintain plasma uniformity under different process conditions, and (b) the helicon ionization mechanism creates higher plasma densities than are possible with ICPs.

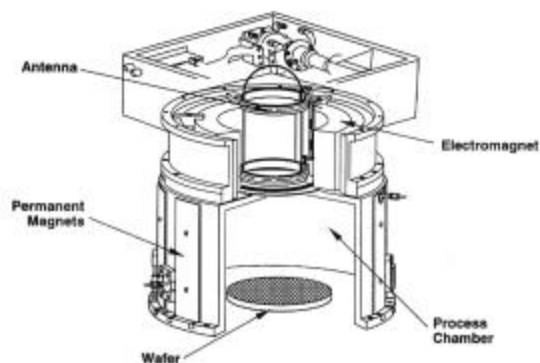


Fig. 1. Schematic of the MØRI source, showing quartz belljar, double-loop antenna, and magnet coils.

This project is to study how the MØRI source can be improved by varying such parameters as the antenna design, the geometry of the discharge chamber and the magnetic coils, etc., and how sensitive the source is to these parameters. To do this requires a transport code to model the plasma equilibrium as well as the helicon code. This cannot be done in a project of this size. In fact, as will be seen, the electron Larmor radius varies from small to large in the process chamber, and to model transport properly would require at least \$1M. Nonetheless, the HELIC code, which is restricted to uniform B-fields, has proved to be a very powerful and useful tool.

## HELIC CODE RESULTS

This code computes antenna coupling and wave propagation for both HELicon and (HEL)ICP discharges. It is based on the theory of Arnush and Chen [3], which reduces the problem to the solution of a second-order differential equation of the form:

$$\mathbf{d}_* \nabla \times \nabla \times \mathbf{B} - k \nabla \times \mathbf{B} + \mathbf{d} k_s^2 \mathbf{B} = u(r) [-\mathbf{d} \hat{\mathbf{r}} \times (\nabla \times \mathbf{B}) + i(\nabla \times \mathbf{B})_r \hat{\mathbf{z}}]$$

(1), where  $\mathbf{d} = \omega/\omega_c$ ,  $\mathbf{d}_* = (\omega + iv)/\omega_c$ ,  $k_s = \omega_p/c$ , and  $u(r)$  is a function containing the radial density gradient (an essential element). The coefficients here have been simplified. The frequency  $\omega$  includes electron-ion and electron-neutral collisions. The plasma is bounded by an insulating cylinder of radius  $a$ , and the antenna is a current sheet at radius  $b \geq a$ . The plasma can have a finite length  $L$ , but axial gradients in  $\mathbf{B}_0$  and  $n$  are neglected. The first term, which arises from inclusion of finite electron mass, introduces a second wave, called the Trivelpiece-Gould (TG) mode, which is coupled to the helicon (H) wave at the boundary and is required by the boundary conditions. The TG mode is mainly electrostatic with short radial wavelength and provides most of the damping. Thus, the theory predicts deposition of wave energy in two regions: near the boundary by the TG mode, and in the interior by the H wave. Though not needed here, much of the work involved finding a new algorithm for handling  $\mathbf{B}_0$ 's above about 300G, where numerical difficulties arose.

Unless stated otherwise, the results shown here are for typical MØRI parameters  $a = 5\text{cm}$ ,  $b = 5.5\text{cm}$ ,  $L = 25\text{cm}$ ,  $T_e = 3\text{eV}$ ,  $p = 3\text{mTorr}$  of argon, and antenna length  $L_a = 11\text{cm}$ . The plasma density is flat, with a roll-off near the edge ( $s=2$ ,  $t = 6$  in Ref. 3 notation.). Figure 1 shows the device, and Fig. 2 shows contours of constant antenna loading (plasma resistance) in  $\Omega$ 's.

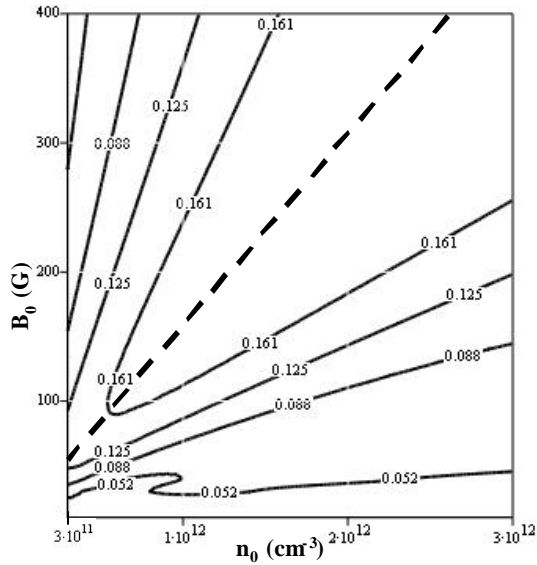


Fig. 2. Contours of constant loading in  $n - B$  space.

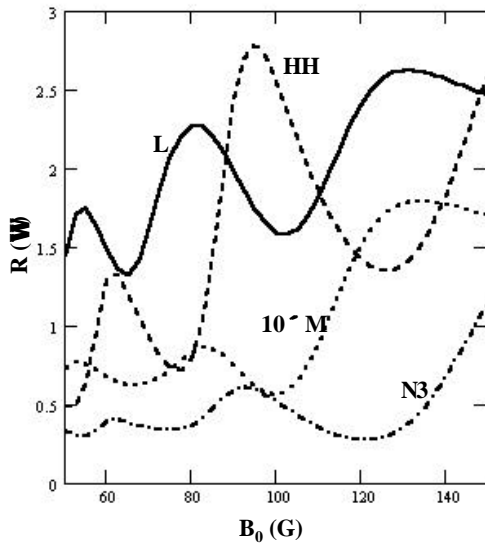


Fig. 3. Antenna loading vs.  $B_0$  for various antennas: MØRI (M), Nagoya Type 3 (N3), half-wavelength helical (HH), and a single-loop  $m = 0$  (L). The MØRI data are multiplied by 10.

Maximum loading  $R$  occurs along the dashed line, showing a linear  $n - B$  relationship reminiscent of the old helicon theory without TG modes. This “ridge”

can be used to design the magnetic field for any desired density. Figure 3 shows  $R$  vs.  $B_0$  for different antennas. Note that the MØRI antenna is by far the worst of the four. Its  $R$  value is sensitive to antenna length at low fields.  $R$  by itself, however, is not proportional to the absorbed power, since the input power is constant. Low  $R$  only means that the parasitic losses are larger.

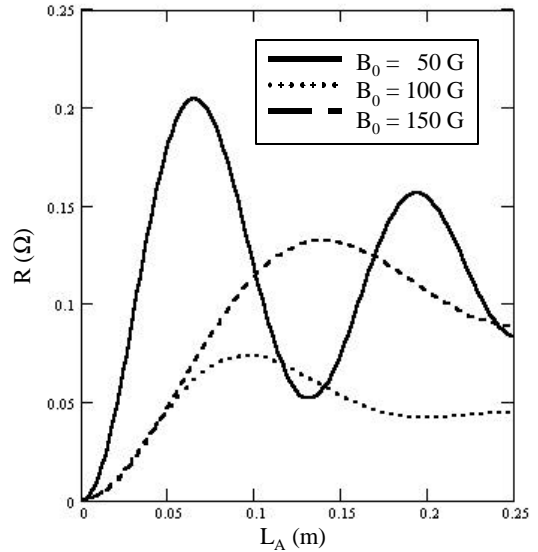


Fig. 4. Loading resistance vs. loop separation.

Figure 4 shows the sensitivity to MØRI antenna length, and Fig. 5 shows the radial distribution of power absorption for different size belljars. The two peaks for the H and TG modes can be seen. As the source diameter is increased to accommodate larger wafers, the power is not delivered only to the surface; it reaches the axis even in a wide source.

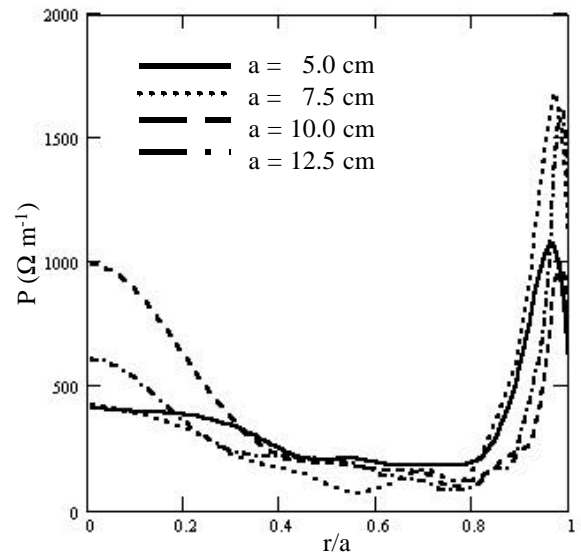


Fig. 5. Power absorption vs. radius for various tube sizes. Note that the abscissa is normalized to the tube radius.

Figure 6 shows how the  $k$ -spectrum of excited axial modes changes with magnetic field. Waves at the dominant  $k$ 's can reflect off the ends of the source and cause interference effects. This erratic behavior can be avoided if the source is sufficiently short or long.

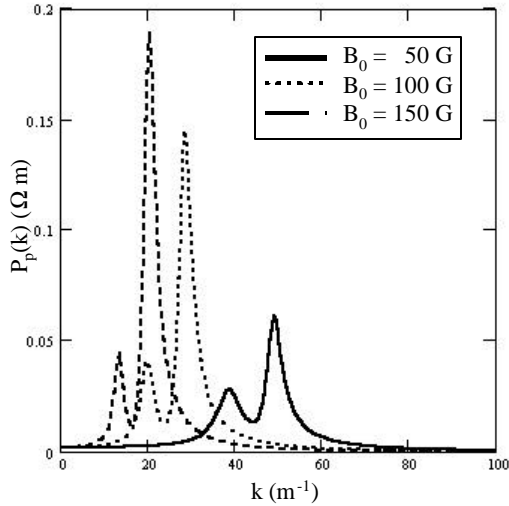


Fig. 6. Spectrum of excited wavenumbers for a single-loop antenna and for various magnetic fields at  $n = 10^{12} \text{cm}^{-3}$ .

### MAGNETIC FIELD DESIGN

The two concentric magnet coils seen in Fig. 1 can be adjusted independently to vary the magnetic field pattern. This flexibility is used to flatten the density profile at the wafer level. To see how this works, we have computed the field pattern for a scaled up model with a 50-cm diameter outer coil used for processing 300-mm wafers. These are shown in Figs. 7 and 8 for four different coil current ratios (CCRs). This is the ratio of outer coil to inner currents, the inner coil having about 3 times as many turns.  $\text{CCR} = 1$  corresponds

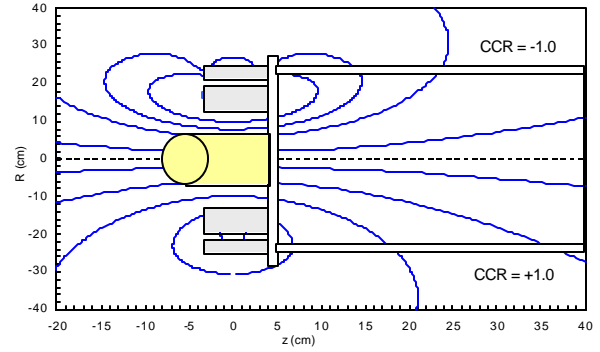


Fig. 7. Field patterns for  $\text{CCR} = +1$  and  $-1$  in the 300-mm system (turned sideways).

to a normal single coil. With the outer coil reversed in  $\text{CCR} = -1$ , the field is not appreciably changed. However, with  $\text{CCR} = -2$ , only the field lines very close to the axis can reach the wafer, and at  $\text{CCR} = -3$  the plasma is spread out rapidly as it leaves the source. Electrons confine the plasma only in the strong-field region. When their Larmor radii become large, the plasma diffuses isotropically. The CCR can be adjusted so that the field is almost zero at the wafer. For instance, at a wafer 30 cm downstream from the

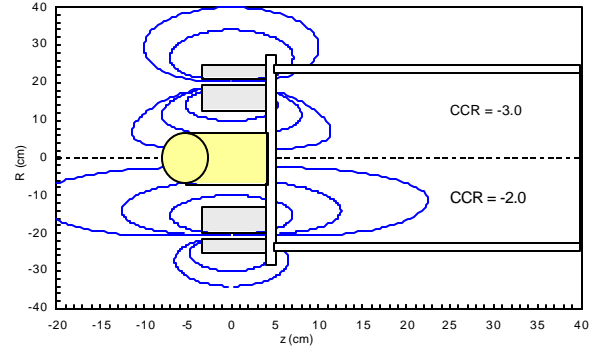


Fig. 8. Field patterns for  $\text{CCR} = -2$  and  $-3$ .

midplane of the coils, the magnitude of  $\mathbf{B}_0$  is shown in Fig. 9 across a diameter. The field there can be nulled out at a given radius by adjusting the CCR, and  $|\mathbf{B}|$  can easily be kept below 2G for 100G in the source. If a larger field is permitted, the field shape can be used to correct for a convex or concave density profile.

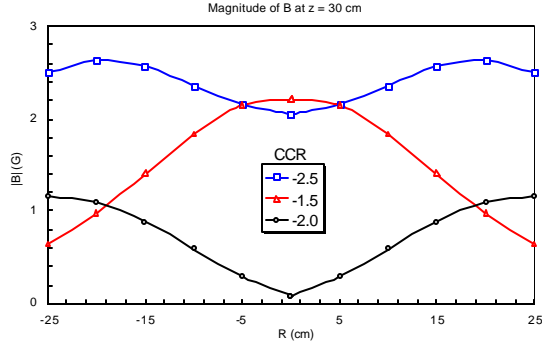


Fig. 9. Magnetic field strength 30 cm from the coil center for different CCRs, for 100G in the source region.

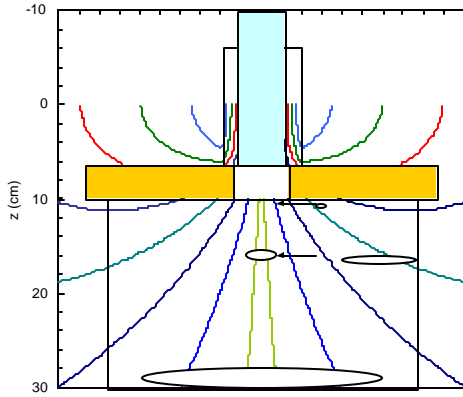


Fig. 10. Electron Larmor radii in a rapidly diverging field.

In a previous experiment, it was found that rapidly diverging field lines can cause plasma to be scraped off by the flange before reaching the main chamber (Fig. 10). Thus, large negative CCRs must be used with caution, lest most of the plasma production be lost. Also shown in Fig. 10 is the size of the electron Larmor diameters for 100G in the source. It is seen that this becomes so large that individual electron orbits have to be followed in numerical modeling. Fig. 10 also shows that plasma must drift out of the tube at the Bohm velocity, since the aperture acts like a wall sheath if there are few ions going back into the source.

### SKIN DEPTH IN WEAK MAGNETIC FIELDS

Just when does an ICP discharge become a helicon discharge? In an axisymmetric ICP, the RF fields have  $\mathbf{E}$  in the  $\mathbf{q}$  direction and  $\mathbf{B}$  in the  $z$  direction, and their penetration is described by the formula

$$B_z = A I_0(T r), \quad T = k_s (1 + \mathbf{u} / \mathbf{w})^{-1/2},$$

where  $k_s = \omega_p / c$ . When a small DC field  $\mathbf{B}_0$  is added in the  $z$  direction, this formula cannot be modified easily, since the electrons now have an  $\mathbf{E}_0 \times$

$\mathbf{B}_0$  drift in the  $r$  direction, creating a radial  $E_r$ . Rather than starting over, we can simply take the exact helicon formula of Eq. (1) to the small- $\mathbf{B}_0$  limit. Both roots then coalesce, and in plane geometry, we have

$$k_x^2 = \mathbf{b}^2 - k^2, \quad \mathbf{b} = \frac{k}{2d_1} + \left( \frac{k^2}{4d_1^2} - \frac{d_2 k_s^2}{d_1} \right)^{1/2}, \quad (2)$$

where the  $\delta$ 's are essentially  $\omega/\omega_c$  but are exact complex numbers including collisions, ion motions, and displacement current and given in Ref. 3 in terms of the cold-plasma dielectric elements. We have written  $\mathbf{b}$  in a form that remains determinate in the limit  $\omega_c \rightarrow 0$ . One would expect that  $\mathbf{B}_0$  would restrict the  $\mathbf{q}$  motion of the electrons that shield out the RF B-field. However, Eq. (2) shows that when  $k \rightarrow 0$ ,  $k_x \rightarrow k_s$ , so that there is no effect of the  $\mathbf{B}_0$ -field. (Without collisions, the skin depth is the collisionless skin depth  $1/k_s$ .) The reason is that the charge build-up due to the  $\mathbf{E}_0 \times \mathbf{B}_0$  motion causes an  $\mathbf{E}_p \times \mathbf{B}_0$  drift which just restores the shielding current  $j_q$ . When  $k = k_z \neq 0$ , however, the electrostatic charges can bleed away by electron streaming along  $\mathbf{B}_0$ . When  $k$  is finite, the skin depth indeed increases with  $\mathbf{B}_0$ , but not continuously. At a critical  $\mathbf{B}_0$ , the square root in Eq. (2) becomes real, and a propagating wave is abruptly generated. This is illustrated in Figs. 10-12, computed with proper collisions for  $n = 10^{12} \text{ cm}^{-3}$ ,  $KT_e = 3\text{eV}$ , and  $p = 3\text{mTorr}$  of argon.

In Fig. 11 we see that there is a slight change in skin depth as  $\mathbf{B}_0$  is increased, but there is a sudden jump to a propagating wave when the square root in Eq. (2) becomes real. In Fig. 12, with  $k = 0$ , the skin depth is not changed until very large fields  $\mathbf{B}_0$  are applied, and then the change is not monotonic because it is all due to collisions. Thus there is no continuous transition between ICPs and HWS plasmas. In practice, there is an entire spectrum of  $k$ 's generated by the antenna, and the HELIC code must be used to track this transition.

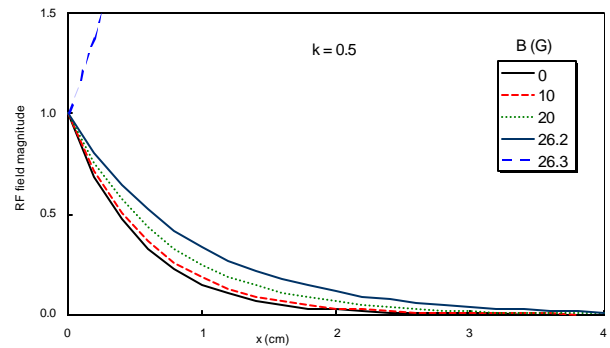


Fig. 11. Radial field distribution with increasing  $\mathbf{B}_0$  for  $k = 0.5 \text{ cm}^{-1}$ .

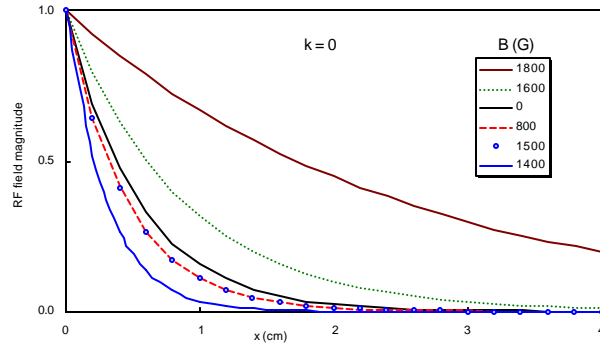


Fig. 12. Radial field distribution with increasing  $B_0$  for  $k = 0$ .

The MØRI source was originally designed after a few months of trial and error, with only a weak theoretical basis. Our understanding of helicon discharges has advanced significantly in the past six years, culminating with the discovery of the importance of TG-mode coupling. The HELIC code facilitates application of these results. The relation between helicon and the popular ICP sources has been clarified. What is needed now is a finite-Larmor-radius transport code which can solve for the equilibrium profiles given the energy deposition profile.

- 
- [1] G.R. Tynan, A.D. Bailey III, G.A. Campbell, R. Charatan, A. de Chambrier, G. Gibson, D.J. Hemker, K. Jones, A. Kuthi, C. Lee, T. Shoji, and M. Wilcoxson, *J. Vac. Sci. Technol. A* **15**, 2885 (1997).
- [2] T.P. Schneider, W.W. Dostalík, A.D. Springfield, and R. Kraft, *Plasma Sources Sci. Technol.* **8**, 397 (1999).
- [3] D. Arnush and F.F. Chen, *Phys. Plasmas* **5**, 1239 (1998).